UC Berkeley
UC Berkeley Previously Published Works

Title

Structural and Chemical Evolution of the Layered Li-Excess LixMnO3 as a Function of Li Content from First-Principles Calculations

Permalink

https://escholarship.org/uc/item/42p47834

Journal

Advanced Energy Materials, 4(15)

ISSN

1614-6832

Authors

Lee, Eunseok
Persson, Kristin A

Publication Date

2014-10-01

DOI

10.1002/aenm.201400498

Peer reviewed

Structural and Chemical Evolution of the Layered Li-Excess Li$_x$MnO$_3$ as a Function of Li Content from First-Principles Calculations

Eunseok Lee* and Kristin A. Persson

Li$_2$MnO$_3$ is a critical component in the family of "Li-excess" materials, which are attracting attention as advanced cathode materials for Li-ion batteries. Here, first-principle calculations are presented to investigate the electrochemical activity and structural stability of stoichiometric Li$_x$MnO$_3$ ($0 \leq x \leq 2$) as a function of Li content. The Li$_2$MnO$_3$ structure is electrochemically activated above 4.5 V on delithiation and charge neutrality in the bulk of the material is mainly maintained by the oxidization of a portion of the oxygen ions from O^{2-} to O^{1-}. While oxygen vacancy formation is found to be thermodynamically favorable for $x < 1$, the activation barriers for O^{2-} and O^{1-} migration remain high throughout the Li composition range, impeding oxygen release from the bulk of the compound. Defect layered structures become thermodynamically favorable at lower Li content ($x < 1$), indicating a tendency towards the spinel-like structure transformation. A critical phase transformation path for forming nuclei of spinel-like domains within the matrix of the original layered structure is proposed. Formation of defect layered structures during the first charge is shown to manifest in a depression of the voltage profile on the first discharge, providing one possible explanation for the observed voltage fade of the Li-excess materials.

1. Introduction

The cathode material constitutes a major component of Li-ion batteries (LIB) and a key factor in determining their energy density. Since the commercially successful debut of the layered structure LiCoO$_2$, several other cathode materials based on the spinel or olivine structures have been proposed.[1] Despite recent progress and commercialization of these materials, the volumetric energy density and cost of Li-ion batteries is still insufficient to achieve wide adoption of electric transportation. Recently, the composite or solid-solution Li-excess materials, have been highlighted for their high initial capacity; greater than 200 mAh g^{-1}.[2–4] However, the commercialization of the Li-excess materials have been delayed due to insufficient cycling performance, voltage fade, long-time structural degradation, slow rate capability, etc.[4–8] While these materials have

been under intense investigation the last 10 years, see e.g., ref. [2–12] and references therein, the underlying relationship between the electrochemical behavior, chemical composition, structural stability and cycling deficiency (e.g., capacity and voltage fade) is still under debate.

The layered Li$_2$MnO$_3$ is a critical component in the Li-excess materials and believed to be responsible for the high-voltage (4.4–5 V)[13] portion of the capacity delivered. In particular, its 2:1 ratio of Li to Mn suggests high theoretical specific capacity (maximum capacity of 460 mAh g^{-1}) as compared to other cathode materials which have 1:1 and 1:2 cation ratio, e.g., layered LiMO$_2$ and spinel LiM$_2$O$_4$ (M = Co, Ni, Mn, ...). However, there is still uncertainty as to the chemical origin of the electrochemical activity of Li$_2$MnO$_3$ as well as its structural evolution during cycling.[6,12,14–17] The delivered capacity and performance at a given temperature and rate is highly dependent on the synthesis procedure and possible additional post-synthesis treatments (such as acid leaching, oxidation, etc.)[14] resulting in differing particle sizes, porosity, surface area, materials defects (stacking faults etc).[18–21] While solid-state synthesized micrometer-scale Li$_2$MnO$_3$ shows very limited electrochemical activity, the nanometric material can deliver up to 200 mAh g^{-1}.[12,15,18] Fully lithiated Li$_2$MnO$_3$ exhibits highly oxidized Mn^{4+}, and further oxidization of Mn has not been conclusively shown to occur.[12] Thus, alternative or complementary processes such as concurrent oxygen release,[17] surface oxygen release coupled with Mn migration,[6] anion oxidation,[6,9,22–25] decomposition,[26] and ion exchange[26,27] have been proposed. Furthermore, increasing evidence suggests that the majority of the Li-excess materials (with a varying degree of Li$_2$MnO$_3$ content) undergo a partial phase transformation from the layered structure to layered with spinel-like domains.[3,12,15,19] This transformation is well-documented[28–30] for Mn-rich layered structures LiMO$_2$ materials, but is less understood for the Li$_2$MnO$_3$ compound.[12] Structural degradation in Li$_2$MnO$_3$ would impact the electrochemical as well as mechanical behavior of the composite electrode.

To increase our knowledge of the Li-excess materials, in this study we focus on the layered Li$_2$MnO$_3$ component, particularly to elucidate its electrochemical behavior, stability and possible accompanying phase transformations as a function of Li

Dr. E. Lee, Dr. K. A. Persson
Environmental Energy Technologies Division
Lawrence Berkeley National Laboratory
Berkeley, CA 94720
E-mail: eunseoklee@lbl.gov

content. While there have been numerous experimental studies of this material, particularly as a component in the family of Li excess cathodes, previous theoretical studies have been few[11,23] and limited to the specific delithiation mechanism of the material pertaining to the sequence of Li removal and Li mobility. In our work, we utilize the strength of first-principles calculations to control and study the material in a range of model situations, with the aim to elucidate its chemical and structural evolution as a function of Li removal. The voltage profiles are obtained from the calculations and compared with experimental observations.[18] From our work, we find that Li ions can be extracted from Li_2MnO_3 above 4.5 V and that the charge is balanced primarily by oxidization of a portion of the oxygen ions. For $x > 1$, we find that the layered Li_xMnO_3 structure is thermodynamically stable, while for $x < 1$ structures with varying degrees of defect domains are favored. Furthermore, we show an evident voltage profile depression between the first charge and discharge, originating from the expected structural transformation of the pristine material to a more stable structure with Mn defect domains. As a function of Li content, we examine Mn migration from the Mn-layer into the Li-layer as a first towards forming defect spinel-like domains. The energy barrier of Mn migration is very high at high Li content, but decreases with delithiation and, for low overall as well as low local Li content, allows for rapid transformation. These results suggest that Mn migration into the Li layer is possible for low Li content Li_xMnO_3 yielding an increased formation of defect domains with increasing charge. Finally, we find that, while oxygen vacancies are thermodynamically favorable for $x < 1$, the oxygen migration barriers remain too high for bulk transport throughout the Li composition range. However, oxygen release in the surface region of the material is deemed feasible.

2. Computational Model and Methodology

The crystal structure of Li_2MnO_3 is illustrated in **Figure 1**. It has a layered structure with ABC oxygen stacking (O3-type), similar to other layered electrode materials, e.g., $LiMO_2$ (M = Co, Mn, Ni). However, Li_2MnO_3 contains additional Li ions in the Mn-layer: one Li ion per two Mn ions is positioned at the 2b sites. In perfectly ordered Li_2MnO_3, the Mn and Li occupy different sublattices. However, to explore the entire chemical space accessed by a possible phase transformation to defect
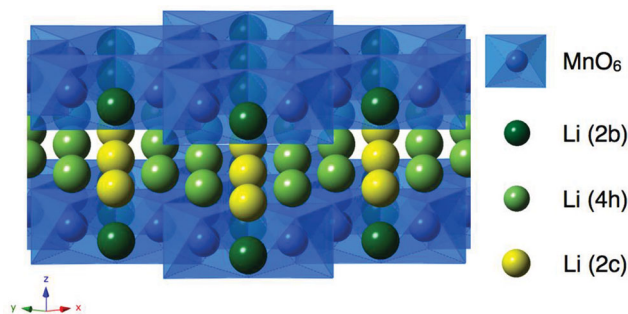
spinel-like structures, we allow the Mn, Li, and vacancies (Va) to be located at any of the octahedral sites. By comparing the energy of all possible cationic configurations (within the same oxygen framework), we can identify the stable states and analyze the impact of lithiation/delithiation on the most favorable ionic arrangement.

To increase the efficiency of our approach and avoid calculating every atomic configuration, we used a (ternary) cluster expansion with the degree of freedom of Li/Mn/Va at each lattice site to systematically search for stable chemical configurations. Few ternary cluster expansions have been reported in the literature[31,32] as they are notoriously hard to converge and complicated to implement. In this work, we assign 1, –1, and 0 to represent Li, Mn, and Va occupation of a site, respectively. Hence the atomic configuration of the compound can be represented as a vector of occupation variable σ. Using this nomenclature, the energy of n-lattice sites system can be expressed by the expansion of the occupational variables.

$$E(\{\sigma_1, \cdots \sigma_1\}) = \sum_\alpha \sum_{(s)} V_\alpha^{(s)} \phi_\alpha^{(s)} (\{\sigma_1, \cdots \sigma_1\}) \qquad (1)$$

where α indicates each cluster, (s) is permutation of {1, 2} with duplicates by the number of lattice site in α, V_α is called the effective cluster interaction (ECI), and φ_α is the cluster function defined as

$$\phi_\sigma^{(s)}(\{\sigma_1, \cdots \sigma_1\}) = \phi_{s1}(\sigma_1) \cdots \phi_{s|\alpha|}(\sigma_{|\alpha|}) \qquad (2)$$

where $|\alpha|$ is the number of lattice site in α and φ_{s1} is the s1-th Chebychev polynomial. Once the ECIs are fitted, they are used to predict the energy of atomic configurations that are not included in the fitting. The ECIs are obtained by the iteration of fitting-predicting (see e.g., ref. [31,32] for more details), until the predicted lowest energy states (ground states) remain the same irrespective of the data set used and the error of prediction is small.

The compound energies were calculated by the zero-temperature density functional theory (DFT) within the Perdew-Burke-Ernzerhof parametrization of the generalized gradient approximation[33,34] as implemented in the Vienna ab initio Simulation Package (VASP).[35–38] Furthermore, projector augmented wave (PAW)[39,40] potentials were used. During the relaxation, both the volume and the shape of the supercell were optimized and a high cutoff energy (520 eV) together with a k-point sampling, which was adjusted depending on the size of the supercell, ensured an energy convergence of 1 meV per atom. Spin-polarized calculations were performed to calculate the energy using different magnetic orderings to achieve the lowest energy. The GGA+U scheme (with a U of 4.5 eV for Mn)[41] was employed to account for the electron localization around the ions to calculate the accurate oxidation states of Mn and O. A few benchmark calculations using the GGA, GGA+U, and HSE (Heyd-Scuseria-Ernzerhof) schemes for the same ionic configurations were performed to confirm the adequacy of the GGA+U scheme in this work. For the HSE scheme,[42] which adopts the hybrid Hartree-Fock/DFT functionals and is believed to improve the description of the localized electron states,[43] two parameters, one to separate the short and long range in the exchange functional and the other to specify the fraction of exact exchange,

Figure 1. The crystal structure of Li_2MnO_3. For improved visualization of the framework, the oxygen atoms are hidden. Lattice sites are indexed following the Wyckoff positions.

Legend: MnO₆; Li (2b); Li (4h); Li (2c)

www.MaterialsViews.com

ADVANCED
ENERGY
MATERIALS
www.advenergymat.de

FULL PAPER

were set to 0.2 and 0.25, respectively.[44] The oxidation state of each ion was determined by integrating the local magnetic moment within the Wigner-Seitz radius for each ion as given in the PAW potentials. For the calculation of the activation energy barriers, we used the nudged elastic band method[45] as implemented in the VASP with eight intermediate images between the two end states. A supercell size of $2 \times 2 \times 3$ containing 24 f.u. (144 atoms), was deemed large enough to ensure convergence and exclude the interference from self-images.

3. Results and Discussion

3.1. Delithiation Mechanism

As we carefully mapped out the Li_xMnO_3 chemical space, including Mn defects and structural deformations associated with the different Li/Va/Mn decorations across the two layers, we found that many configurations with migrated Mn exhibited significantly different relative lattice parameters as compared to the original layered structure. This is expected, as we are exploring structures in-between the layered and the spinel structure space. To arrive at ECIs that correctly capture the ionic interactions in the layered Li_xMnO_3 structure, we included only the structures in the fitting where the ionic configurations were compatible (e.g., small structural relaxations) with the original structure parameters. Specifically, we considered the structure deformed when the deviation between the unrelaxed and relaxed structure exceeded either 7%, in relative lattice parameters, or 5% in relative angles. In total, 183 structures, whereof 85 structures retained the original layered cell shape (denoted "layered") and 98 structures did not (denoted "defect layered"), were calculated and analyzed. An error of prediction of 10 meV per formula unit (f.u.) was obtained for the 'layered' set of structures, which is less than 1% the spectrum of energy per f.u. of Li_2MnO_3.

The DFT calculation results are shown in **Figure 2**, where the formation energy, defined as $E_f(x) = E(Li_xMnO_3) - (1 - x/2)E(MnO_3) - x/2E(Li_2MnO_3)$, is plotted to clearly distinguish the intermediate stable states. The blue dots indicate the data sets which retained the layered structure shape during the structural relaxation (layered), while the red dots indicate the compounds where some Mn ions reside in the Li layer and the structure shape deviates significantly from the layered (defect layered). Interestingly, we note that many of the defect structures were actually predicted as stable by the cluster expansion that only included layered structures, indicating that the information about the structural instability as Li is removed is embedded in the atomic interactions of the original structure. Assuming that no transformation occurs during the delithiation, the convex hull of layered structures exhibits two intermediate stable ground states at $x = 0.5$ and $x = 1$, which lead to three two-phase reaction regions: between $x = 0$ and $x = 1$, between $x = 1$ and $x = 0.5$, and between $x = 0.5$ and $x = 0$. However, particularly at high Li content ($1 < x < 2$), there are several states very close to the convex hull, indicating a possibility towards solid solution-like behavior at the beginning of charge. From the ionic configuration at each intermediate stable state, we can extract the likely process for
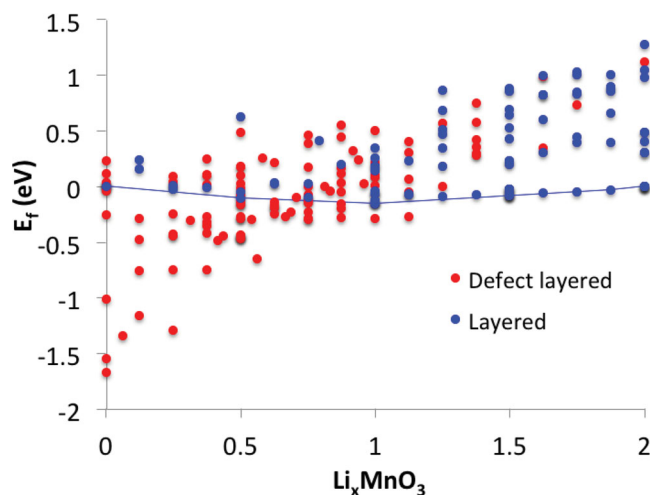
Figure 2. The formation (DFT) energy of Li_xMnO_3 where the red and blue dots indicate the structures termed defect layered and layered, respectively. The blue line indicates the convex hull of the data sets with layered structures.

Li extraction in Li_xMnO_3 from a thermodynamic perspective during the first charge: first, Li at the 2b site (in the Mn-layer) and Li at the 2c site, then a fraction of the Li ions at the 4 h site are extracted forming a specific Li/Va ordering, and finally all the remaining Li ions at 4 h site are extracted (see illustration in the Supporting Information). These results agree with the general conclusions in previous computational works[11,23] predicting a sequence of Li extraction from the Li-layer and the Mn-layer at $x = 1$. However, we note a slight difference for the composition range $1 < x < 2$ where ref. [11] indicated a few intermediate stable states, which we found to be de-stabilized by the new layered ground state at $x = 1$ identified in this work.

For every extracted Li^+ ion, the charge of one electron should be compensated. To analyze whether these electrons are primarily originating from orbitals associated with Mn and/or O, we calculated the charge of each ion from the magnetic moment. Cognizant of the fact that the chosen DFT functional determines the degree of localization and charge sharing between the cations and anions, we employed the GGA, GGA+U and the HSE scheme for a range of structures near the convex hull. The results are given in **Table 1**. A priori, we would

Table 1. Predicted manetic moments (unit: μB) of Mn and O, using GGA, GGA+U, and HSE formulation of DFT, as a function of Li content. The magnetic moment calculation is sensitive to the Wigner-Seitz radius and unparallel component of angular momenta. The change of ≈ 0.7 μB in the magnetic moment of oxygen compared to the Mn (GGA+U/HSE) indicates that the main redox activity is on the anion specie.
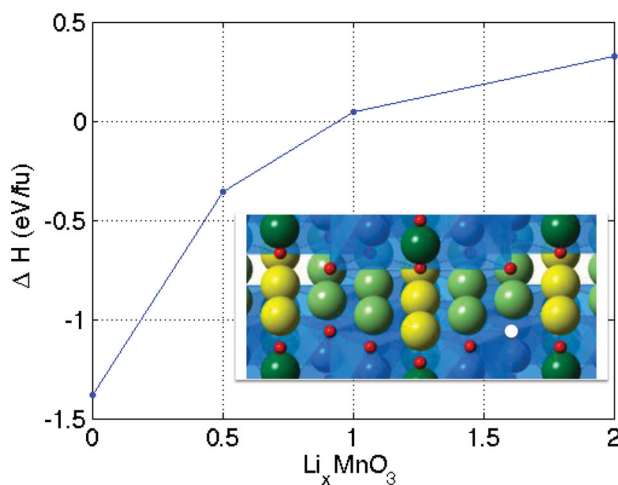
		$x = 0$	$x = 0.5$	$x = 1$	$x = 1.5$	$x = 2$
Mn mag.	GGA+U	3.27	3.16	3.16	3.23	3.22
	GGA	0.02	0.08, 1.65	2.04	2.43	2.76
	HSE	3.07	2.94	2.91	2.90	2.95
O mag.	GGA+U	–0.20,–0.70	0, –0.70	–0.37	–0.21	–0.08
	GGA	0.00	0.00	0.00	0.00	0.00
	HSE	–0.20,–0.78	–0.04,–0.60	–0.04,–0.75	–0.11,–0.19	–0.01

expect that the GGA+U and the more computationally expensive HSE scheme, which uses Hartree-Fock hybrid functionals to provide better representations of the electron distribution in a Mn-O system, compared to the GGA. Indeed, Table 1 shows a high level of consistency between the GGA+U and HSE results which lends credibility to the results. From the table, we observe that both the HSE and GGA+U indicate that Mn remains largely in the 4+ oxidation state throughout the entire range of x, in agreement with recent findings by Rana et al.[12] Instead, charge neutrality is maintained by a fraction of oxygen atoms changing their oxidation state from O^{2-} to O^{1-} as Li is removed, in support of experimental reports on Li excess materials such as $Li_{1.2}Mn_{0.54}Co_{0.13}Ni_{0.13}O_2$ and $Li_2Ru_{1-y}Sn_yO_3$.[6,24,46]

Oxygen release has been suggested as another possible mechanism for charge compenzation in Li_2MnO_3 during delithiation.[29,47,48] To examine the thermodynamic stability of oxygen we calculated the oxygen vacancy formation enthalpy ΔH_O, defined as

$$\Delta H_O(x) = E(Li_xMnO_{3-\delta}) + \delta/2E(O_2) - E(Li_xMnO_3) \qquad (3)$$

To correct for self-interaction errors within DFT, we used $E(O_2)$ from ref. [49], where the energy is calibrated by a comparison between DFT calculations and experimental measurements of the formation enthalpies for several oxides. For each chosen composition ($0 < x < 2$) we examined the formation of an O^{2-} or O^{1-} (if applicable) vacancy as a function of local cation environment and symmetry and present only the lowest energy, most favorable, case. **Figure 3** shows that oxygen vacancy formation is thermodynamically favorable when the Li content is lower than $x \approx 1$, similar to previous findings.[50] However, oxygen evolution is also controlled by kinetics if oxygen vacancies created at the surface are to be distributed within the bulk of the material. To determine whether the thermodynamic instability towards oxygen release is enabled by oxygen mobility in the bulk of the structure, we calculated the energy barrier of oxygen ion diffusion in Li_xMnO_3 via a vacancy-mediated mechanism. The nudged elastic band method was used to obt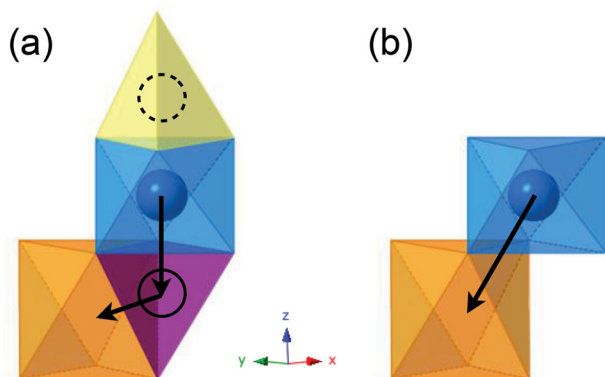ain the energy profile during the jump of an oxygen vacancy to one of the nearest neighbor oxygen sites. The lowest activation energy barriers were predicted to be 3.9 eV at $x = 0$, 2.0 eV at $x = 0.5$, 0.9 eV at $x = 1$, and 2.1 eV at $x = 2$. At $x = 1$, two species of oxygen are present: and O^{1-}. We specifically note that the lowest barrier, at $x = 1$, for an O^{1-} to migrate to the vacancy is 0.9 eV while the same hop for an O^{2-} is 2.3–4.0 eV depending on its position and hopping direction. The results are intuitive, as a lower charge of the migrating ion will reduce its electrostatic interaction with the surrounding ions. Clearly, there is a strong thermodynamic driving force for oxygen evolution from this material at high charge, but it is kinetically impeded. The activation barrier of Eb ≈ 0.9 eV at $x = 1$ for O^{1-} migration indicates the possibility of a small but nonzero amount of oxygen evolution at room temperature,[51,52] most likely at the surface where undercoordination, disorder and strain effects may facilitate the migration.[53] However, the significant bulk oxygen vacancy migration that is required to compensate for the charge process and continuous cycling of Li_2MnO_3 is not supported by the results in this work.

3.2. Phase Transformation

In the low Li content region ($x < 1$), we note that all low energy structures are defect layered (red dots in Figure 2), supporting experimental evidence that Li_xMnO_3 and related materials are far from equilibrium when activated.[6,12] In all defect layered structures, a fraction of Mn ions are displaced to the Li-layer which implies a strong tendency towards Mn migration into the Li-layer. At charge beyond $x = 1$, clearly, the layered structure experiences a frustration and thermodynamic driving force towards cation migration. However, many structures remain in metastable configurations despite a thermodynamic instability towards a more stable crystal structure, due to kinetic limitations. In this case, the structural transformation requires Mn^{4+} to move, which is likely impeded by strong interactions with surrounding ions.[54] To examine this issue, we investigated Mn migration in the Li_xMnO_3 structure as a function of Li content. When a Mn ion migrates into the Li-layer, it aims to occupy the nearest octahedral site in the Li-layer. We considered two migration paths as illustrated in **Figure 4**, which we denote the "Dumbbell Path" and the "Edge Path". The Dumbbell Path is well-known in the literature[28–30,55,56] and has been suggested as the most probable transition metal migration path in previous first-principles calculations studies pertaining to other layered materials. It is composed of two steps: 1) the Mn ion, flanked by one Li in the neighboring tetrahedral site, migrates into the nearest tetrahedral Va site in the Li-layer and then 2) moves, through a face, into the nearest octahedral site in the Li layer. In this study, we also consider another possibility, the Edge Path, in which the Mn migrates into the nearest octahedral site from the Mn layer to the Li layer directly through the connecting oxygen edge. The energy barriers (Eb) for Mn migration are calculated along the two paths for three different Li concentrations. For the Dumbbell Path, only the first step (the dumbbell formation) is examined as this will be rate-limiting.

The results are given in **Table 2**. Following the increased instability of the original layered structure, we observe that E_b overall decreases with delithiation for both paths, which can be

Figure 3. ΔH as a function of x in Li_xMnO_3. The inset figure illustrates an O vacancy (open circle).

Figure 4. Illustration of the two examined paths for Mn migration into the Li-layer: a) the Dumbbell Path, where a dumbbell of Mn (circle)-vacancy-Li (dashed circle) enables a Mn ion at the octahedral site to migrate into the tetrahedral site (purple) and b) the Edge Path.

Figure 5. The energy profile during a Mn migration via the Edge Path at $x = 0$. The points 0 and 9 indicate the initial and final states, respectively. The highlighted oxygen ion (red-star) moves substantially to decrease the distance to the oxygen ions in the red-dashed ellipse.

generally explained by a decrease in electrostatic interactions between the migrating Mn ion and the neighboring Li ions. The high E_b at $x = 1$ and $x = 0.5$ ($E_b > 1$ eV) implies that the Mn migration is kinetically suppressed, despite the strong thermodynamic driving force for the Mn migration (see Figure 2). At $x = 1$ and $x = 0.5$, the Edge Path exhibits a higher E_b than the Dumbbell Path. At $x = 0.5$, the Dumbbell activation energy is 0.7 eV, which is sluggish but feasible at room temperature and, interestingly, at $x = 0$, the Edge Path drops to a very low $E_b = 0.1$ eV enabling fast migration kinetics. This rapid drop is clearly indicative of a more complex, possibly cooperative process. To highlight the significant changes in local atomic environment as the Mn moves, the intermediate steps of Mn migration via the Edge Path at $x = 0$ and the corresponding energy are shown in **Figure 5**. Following the intermediate structure illustrations in Figure 5, we find that when a Mn ion passes through the shared edge between its octahedral start and finish sites, the distance between the oxygen ions along the edge is increased from 2.81 Å to 3.67 Å, providing more space for the Mn to glide through. In particular, the oxygen ion indicated with a red-star (see Figure 5) moves substantially to decrease the distance to the oxygen ions highlighted by the red-dashed ellipse from 2.45 Å to 1.35 Å. Analyzing the charge of the participating ions, we find that the two oxygen ions on the shared edge in the Edge Path both exhibit O^{1-} valence charge, which reduces the interaction with the migrating Mn ion, resulting in the facile deformation of the oxygen environment and a low energy barrier for Mn migration. We believe this cooperative motion, a local stretching and deformation of the oxygen cage concerted with the Mn migration, enables the mobility of the Mn ion to accommodate the driving force (at low Li content) for

Table 2. The calculated activation energy barrier of Mn migration from the Mn-layer to the Li-layer using the Dumbbell Path and the Edge Path.

x	Dumbbell ($O_h \rightarrow T_d$)	Edge
0	1.0 eV	0.1 eV
0.5	0.7 eV	2.0 eV
1	1.9 eV	3.6 eV
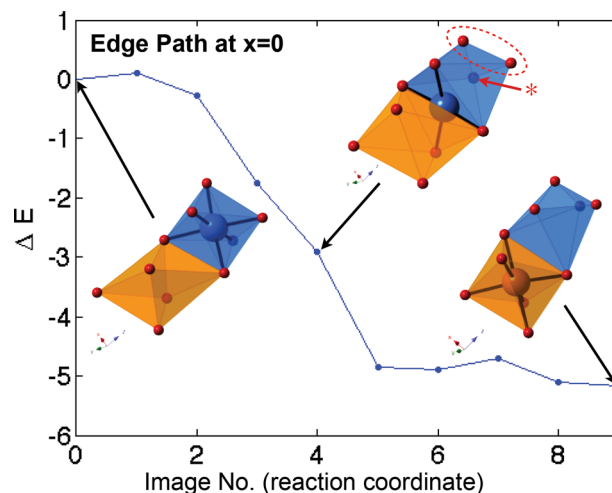
transformation into the significantly more stable defect-layered structure. Also, from Figure 5, we note that the energy profile along the Edge Path, corresponding to the cooperative motion of the oxygens and the Mn, is almost devoid of a barrier and reminiscent of a dynamical instability indicating a possibility of a second-order transition. These transitions are rarely observed, as in practice, most materials will transform through a first-order transformation with a low barrier before the materials becomes mechanically unstable. Curiously, we also observe that the energy barrier for the Dumbbell Path increases between $x = 0.5$ and $x = 0$, which is due to the structure of MnO_3. For low Li content, the Li slab space is significantly reduced from 2.72 Å to 2.36 Å. The reduced interlayer distance results in a significantly smaller-sized, deformed tetrahedral transition site, as compared to the lithiated phases, which increases the energy of the Dumbbell path.

The calculations above were performed on an overall, evenly charged material, close to completely delithiated. We acknowledge that this scenario is unlikely, particularly given the observed low Li mobility in this material.[11,15] Instead, we speculate that, due to chemical and structural inhomogeneities in the material, regions of Li_xMnO_3 locally reaches highly charged states, even though the overall state of charge is $x > 0.5$. Hence, we explore whether it is possible to obtain Mn migration for such a scenario. We calculated the activation energy barrier of a Mn ion migrating from the Mn-layer to the Li-layer (through the Edge Path) in a locally delithiated region, surrounded by the lithiated phase. The $2 \times 2 \times 3$ supercell was prepared to include a MnO_3 phase at the center of a Li_2MnO_3 phase (an illustration is provided in the Supporting Information) and the activation energy barrier was obtained when a Mn in the center region migrates into the Li-layer. The resulting barrier for Mn migration was 0.28 eV; slightly higher than 0.1 eV in the pure MnO_3 phase but still indicative of very facile Mn migration, even for a locally delithiated region in Li_xMnO_3. Thus, in summary, we have confirmed a strong thermodynamic driving force for Mn migration, coupled with very low Mn migration barriers

FULL PAPER
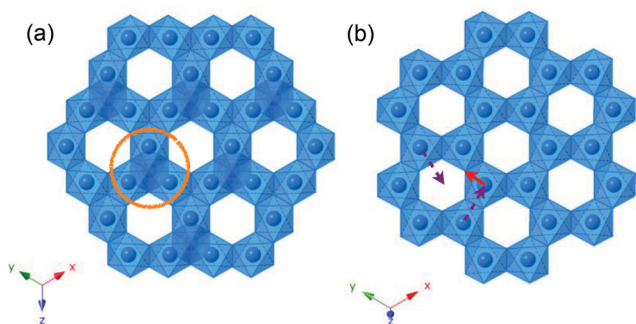
Figure 6. Comparison of Mn-distribution between a) the spinel LiMn$_2$O$_4$ and b) the layered Li$_2$MnO$_3$ structures. For clarity, only Mn ions are shown. The spinel nucleus is composed of four Mn ions, as indicated by the yellow circle. The red arrow in (b) shows the Mn migration into the Li-layer and two purple arrows suggest a path to increase the range of the spinel nucleus.

through the hitherto unsuspected Edge Path coupled with significant local oxygen environment deformation, for both overall low as well as locally low lithium content.

To couple these findings to the possibility of a complete structural phase transition, we examine how the Mn migration into the Li-layer can initiate a transformation to a spinel-like structure. **Figure 6** compares the Mn distribution in layered and spinel structure materials. The major difference between the layered and spinel structures is due to the presence of Mn ions in the Li-layer in the spinel structure, forming a Mn-tetrahedron with the three nearest Mn ions in the Mn-layer. Both structures show a honeycomb network of Mn distribution, although the periodicity vectors are different. Generally, in the layered LiMO$_2$ materials, the center of the honeycomb (the 2b site in Figure 1) is occupied by a transition metal ion. On the other hand, in Li$_2$MnO$_3$, the 2b sites are occupied by the Li ions. As these Li ions are extracted during the delithiation, Li$_x$MnO$_3$ becomes structurally closer to a spinel-like phase. We examined an emerging phase transformation from the layered structure to the defect spinel-like structure based on the formation of a local Mn tetrahedron, which we denote a "spinel-nucleus". Two vertices of the spinel-nucleus can be occupied by Mn ions when one Mn ion migrates into the Li-layer via the Edge Path, which is deemed possible at highly delithiated state (see previous paragraph). To form a complete spinel-nucleus, the other two vertices should also be occupied by Mn ions. Several paths exist for this latter step. Although the activation energy barrier varies depending on the path chosen, we find it can be as low as 0.15 eV for at least one path which is illustrated in Figure 6, at low Li content. In principle, Li migration from the octahedral site to the tetrahedral site should also be considered, as the Li ions in the spinel structure are located at the tetrahedral sites. However, the activation barriers in Table 2 indicate that Mn migration and the formation of the spinel-nucleus occurs at very high charge and very low Li content. Hence, we assume that when the Li ions are reinserted into a partially transformed defect-layered structure, they will be located at the octahedral as well as the tetrahedral sites. The spinel-nucleus formation results in a break of the honeycomb network of Mn distribution and, hence, the transformed domain is limited in size. Thus, our work supports the formation of Mn defects

and spinel-nuclei that will result in the loss of cationic and structural order in the material upon Li extraction.[12,57] The observed thermodynamic as well as kinetic instability of the Li$_x$MnO$_3$ structure, at low Li content, points to a very unstable compound. While we have found compelling evidence for Mn migration, formation of local spinel nuclei and subsequent structural transformations, it is also possible (even likely) that there are other competing structural and chemical ways for the compound to lower its energy. For example, it has been suggested (see e.g., ref. [24] and references therein) that Mn migration from the surface to the bulk (densification) contributes to the degradation of the Li$_2$MnO$_3$ structure upon cycling. An intra-layer Mn migration pattern has not been investigated in our present work and hence cannot be excluded. In summary, examining a complete transformation to the spinel structure is beyond the scope of this paper, but based on our calculations, we believe that spinel nuclei of this kind will form, and result in locally defective domains within the layered matrix.[58]

3.3. Voltage Profile

Finally, to compare our findings, particularly pertaining to a presumed tendency towards defect layered phase transformation, to the experimental evidence of voltage fade[18] we calculate the evolving voltage profile of bulk Li$_x$MnO$_3$ as $V = -\frac{\mu_{Li}^{Cat} - \mu_{Li}^{An}}{Ze}$, where μ_{Li}^{Cat} and μ_{Li}^{An} are the chemical potential of Li at cathode and anode, respectively, Z (= 1) is the valence charge of charge carrier (Li), and e is the electron charge. The voltage profile for the first charge process was obtained by following the convex hull of the formation energy E_f in Figure 2, assuming that the original layered structure stays intact (blue dots). This scenario would correspond to a rigid structure, where the charge compenzation corresponding to the Li removal is mainly enabled by oxygen oxidation, and neither Mn nor O migrates during the charge process. To examine the voltage change as a function of the presumed structural evolution, we explore the structure set, as a function of increasing Li content, where all Mn ions belong to a spinel-nuclei (in a defect layered phase). This scenario corresponds to a discharge where some Mn has migrated, at some point during charge, resulting in more stable, defect-layered phase. We note that we cannot predict which ones of the defect layered structures that would first form, it may be a continuous degradation of the structure as a function of cycling and increased number of migrated Mn, but that the calculated voltage profile for the defect structures should follow the same discharge trend as found in experiments. The results are shown in **Figure 7**, where we compare our calculated voltage profiles to recent experimental works.[18] Note that the charge and discharge process corresponds to decreasing and increasing x, respectively. The blue thick line indicates the voltage profile during the first charge, and clearly indicates that Li$_2$MnO$_3$ is activated at voltages above 4.5 V, in agreement with experiments.[12,18] The discharge (red) curve corresponds to a scenario where the original structure has transformed to a defect phase, where a significant amount of Mn resides in the Li layer. This defect structure is substantially more stable at high charge and less stable at high Li content, compared to the original layered structure. We remark that this structural transition alone
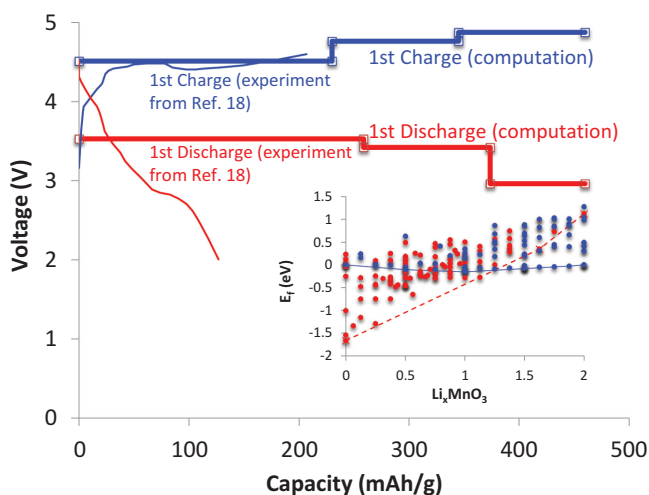
Figure 7. Voltage profiles of Li_xMnO_3 for the first charge (blue lines) and the discharge process (red lines) assuming a structural transformation, originating from Mn migration. The thick lines denote the computational prediction while the thin lines correspond to experimental observations, reproduced from ref. [18]. The inset traces the lowest energy structures for the first charge (blue dash) and subsequent discharge (red dash) processes, reproduced from Figure 2.

(without any presumed oxygen release and/or creation of Mn^{3+}) can give rise to a significant voltage drop – compared to the first charge. The electrochemical activity is still predicted to occur on the anion specie. Comparing to the results of ref. [18], the magnitude of predicted voltage profile and large voltage drop after the first charge process are similar. At high charge (even locally), the defect migration and subsequent local re-arrangement of Mn is predicted to occur rapidly, and reverting back to the original phase at high Li content is kinetically impeded due to high Mn activation barriers (see Figure 2 and 5). Our results indicate that the phase transformation can be suppressed if the voltage is maintained under ≈ 4.7 V and no part of the material reaches high charge or the critical composition $x < 0.5$. We note that the capacity obtained in experiments is significantly less than the theoretical maximum capacity and speculate that an increasing amount of the material becomes inactive, as recently proposed.[12] As investigated in Section 3.2, we propose that, due to inhomogenieties in the sample, local regions of Li_xMnO_3 may undergo higher delithiation than the overall measured state of charge, which will enable partial phase transformation to occur through the suggested Mn migration mechanism. Oxygen loss also has been proposed as an origin of large irreversible capacity loss.[8,10,59] Our computational results summarized in Section 3.1 and 3.2 indicate the oxygen diffusion in the bulk material is impeded and that oxygen release is only likely to occur on the surface where diffusion lengths are short.

4. Conclusion

We used first-principles calculations coupled with a ternary cluster expansion to examine the structural and chemical stability of layered Li_xMnO_3. The material is found to be electrochemically activated at $V > 4.5$ V, in excellent agreement with experiments, through oxidation of a fraction of the oxygen ions from O^{2-} to O^{1-}. Assuming that the material stays structurally intact, we predict a weak two-phase region (possibly solid solution-like behavior at RT) at the beginning of charge, followed by two more pronounced two-phase regions for $0 < x < 1$. However, based on the results in this work, it is deemed unlikely that Li_xMnO_3 remains in the original structure during the first charge process. Among our exhaustive search for more stable defect structures, for $x < 1$, the lowest energy phases all exhibit relative lattice parameters that deviate from the original layered structure with varying degrees of Mn defects present in the Li-layer, indicating a thermodynamic driving force for Mn migration from the Mn-layer into the Li-layer. The Mn^{4+} ion is predicted to move rapidly to the Li layer, if Li is depleted (even locally) through a local cooperative displacement of the oxygen environment. Furthermore, while Li_xMnO_3 exhibits a thermodynamic instability towards oxygen release for $x < 1$, the oxygen migration barriers (even for the O^{1-} specie at high charge) are found to be too high for facile oxygen diffusion in the bulk. However, oxygen release in the surface region of the particles is deemed likely, where local under-coordination and strain may also facilitate the diffusion. Finally, we compare the voltage profile for the first charge of the pristine material, and a subsequent discharge, where we assume that the structure has transformed to a structure with Mn defects in the Li layer. The change in voltage is pronounced, almost 1 V, which qualitatively agrees with experiments. The results suggest that a significant voltage fade can manifest as a result of local Mn migration into the Li layer, effectively creating a defect structure that is more stable at low Li contents.

Supporting Information

Supporting Information is available from the Wiley Online Library or from the author.

[1] M. Thackeray, *Nat. Mater.* **2002**, *1*, 81.
[2] M. M. Thackeray, S.-H. Kang, C. S. Johnson, J. T. Vaughey, R. Benedek, S. Hackney, *J. Mater. Chem.* **2007**, *17*, 3112.
[3] C. Johnson, N. Li, J. Vaughey, S. Hackney, M. Thackeray, *Electrochem. Commun.* **2005**, *7*, 528.
[4] D. Kim, G. Sandi, J. R. Croy, K. G. Gallagher, S.-H. Kang, E. Lee, M. D. Slater, C. S. Johnson, M. M. Thackeray, *J. Electrochem. Soc.* **2013**, *160*, A31.

FULL PAPER

[5] A. van Bommel, L. J. Krause, J. R. Dahn, *J. Electrochem. Soc.* **2011**, *158*, A731.

[6] H. Koga, L. Croguennec, M. Ménétrier, P. Mannessiez, F. Weill, C. Delmas, *J. Power Sources* **2013**, *236*, 250.

[7] B. Xu, C. R. Fell, M. Chi, Y. S. Meng, *Energy Environ. Sci.* **2011**, *4*, 2223.

[8] A. R. Armstrong, M. Holzapfel, P. Novák, C. S. Johnson, S.-H. Kang, M. M. Thackeray, P. G. Bruce, *J. Am. Chem. Soc.* **2006**, *128*, 8694.

[9] A. Ito, K. Shoda, Y. Sato, M. Hatano, H. Horie, Y. Ohsawa, *J. Power Sources* **2011**, *196*, 4785.

[10] Z. Lu, J. R. Dahn, *J. Electrochem. Soc.* **2002**, *149*, A815.

[11] R. Xiao, H. Li, L. Chen, *Chem. Mater.* **2012**, *24*, 4242.

[12] J. Rana, M. Stan, R. Kloepsch, J. Li, G. Schumacher, E. Welter, I. Zizak, J. Banhart, M. Winter, *Adv. Energy Mater.* **2014**, *4*, 1300998.

[13] N. Yabuuchi, K. Yoshii, S.-T. Myung, I. Nakai, S. Komaba, *J. Am. Chem. Soc.* **2011**, *133*, 4404.

[14] C. Johnson, S. Korte, J. Vaughey, M. Thackeray, T. Bofinger, Y. Shao-Horn, S. Hackney, *J. Power Sources* **1999**, *81–82*, 491.

[15] S. F. Amalraj, B. Markovsky, D. Sharon, M. Talianker, E. Zinigrad, R. Persky, O. Haik, J. Grinblat, J. Lampert, M. Schulz-Dobrick, A. Garsuch, L. Burlaka, D. Aurbach, *Electrochim. Acta* **2012**, *78*, 32.

[16] A. Boulineau, L. Croguennec, C. Delmas, F. Weill, *Chem. Mater.* **2009**, *21*, 4216.

[17] A. D. Robertson, P. G. Bruce, *Chem. Mater.* **2003**, *15*, 1984.

[18] S. F. Amalraj, D. Sharon, M. Talianker, C. M. Julien, L. Burlaka, R. Lavi, E. Zhecheva, B. Markovsky, E. Zinigrad, D. Kovacheva, R. Stoyanova, D. Aurbach, *Electrochim. Acta* **2013**, *97*, 259.

[19] S.-H. Park, Y. Sato, J.-K. Kim, Y.-S. Lee, *Mater. Chem. Phys.* **2007**, *102*, 225.

[20] A. Boulineau, L. Croguennec, C. Delmas, F. Weill, *Solid State Ionics* **2010**, *180*, 1652.

[21] T. Penki, D. Shanmughasundaram, N. Munichandraiah, *J. Solid State Electrochem.* **2013**, *17*, 3125.

[22] M. Sathiya, G. Rousse, K. Ramesha, C. P. Laisa, H. Vezin, M. T. Sougrati, M.-L. Doublet, D. Foix, D. Gonbeau, W. Walker, A. S. Prakash, M. Ben Hassine, L. Dupont, J.-M. Tarascon, *Nat. Mater.* **2013**, *12*, 827.

[23] Y. Koyama, I. Tanaka, M. Nagao, R. Kanno, *J. Power Sources* **2009**, *189*, 798.

[24] H. Koga, L. Croguennec, M. Ménétrier, K. Douhil, S. Belin, L. Bourgeois, E. Suard, F. Weill, C. Delmas, *J. Electrochem. Soc.* **2013**, *160*, A786.

[25] J. B. Goodenough, Y. Kim, *Chem. Mater.* **2010**, *22*, 587.

[26] A. Armstrong, A. Robertson, P. Bruce, *J. Power Sources* **2005**, *146*, 275.

[27] A. D. Robertson, P. G. Bruce, *Chem. Commun.* **2002**, *23*, 2790.

[28] J. Reed, G. Ceder, A. V. D. Ven, *Electrochem. Solid-State Lett.* **2001**, *4*, A78.

[29] J. Hong, D.-H. Seo, S.-W. Kim, H. Gwon, S.-T. Oh, K. Kang, *J. Mater. Chem.* **2010**, *20*, 10179.

[30] Y. Shao-Horn, S. A. Hackney, A. R. Armstrong, P. G. Bruce, R. Gitzendanner, C. S. Johnson, M. M. Thackeray, *J. Electrochem. Soc.* **1999**, *146*, 2404.

[31] C. Wolverton, D. de Fontaine, *Phys. Rev. B* **1994**, *49*, 8627.

[32] D. Lerch, O. Wieckhorst, G. L. W. Hart, R. W. Forcade, S. Muller, *Modelling Simulation Mater. Sci. Eng.* **2009**, *17*, 055003.

[33] J. P. Perdew, K. Burke, M. Ernzerhof, *Phys. Rev. Lett.* **1997**, *78*, 1396.

[34] J. P. Perdew, K. Burke, M. Ernzerhof, *Phys. Rev. Lett.* **1996**, *77*, 3865.

[35] G. Kresse, J. Furthmüller, *Comput. Mater. Sci.* **1996**, *6*, 15.

[36] G. Kresse, J. Furthmüller, *Phys. Rev. B* **1996**, *54*, 11169.

[37] G. Kresse, J. Hafner, *Phys. Rev. B* **1994**, *49*, 14251.

[38] G. Kresse, J. Hafner, *Phys. Rev. B* **1993**, *47*, 558.

[39] G. Kresse, D. Joubert, *Phys. Rev. B* **1999**, *59*, 1758.

[40] P. E. Blöchl, *Phys. Rev. B* **1994**, *50*, 17953.

[41] F. Zhou, M. Cococcioni, C. A. Marianetti, D. Morgan, G. Ceder, *Phys. Rev. B* **2004**, *70*, 235121.

[42] A. V. Krukau, O. A. Vydrov, A. F. Izmaylov, G. E. Scuseria, *J. Chem. Phys.* **2006**, *125*, 224106.

[43] T. Tamura, T. Ohwaki, A. Ito, Y. Ohsawa, R. Kobayashi, S. Ogata, *Modelling Simulation Mater. Sci. Eng.* **2012**, *20*, 045006.

[44] V. L. Chevrier, S. P. Ong, R. Armiento, M. K. Y. Chan, G. Ceder, *Phys. Rev. B* **2010**, *82*, 075122.

[45] G. Mills, H. Jónsson, G. K. Schenter, *Surface Science* **1995**, *324*, 305.

[46] M. Sathiya, K. Ramesha, G. Rousse, D. Foix, D. Gonbeau, A. S. Prakash, M. L. Doublet, K. Hemalatha, J. M. Tarascon, *Chem. Mater.* **2013**, *25*, 1121.

[47] D. Y. Yu, K. Yanagida, *J. Electrochem. Soc.* **2011**, *158*, A1015.

[48] Z. Xu, J. Wang, K. Zhang, H. Zheng, Z.-X. Dai, J. Gui, X.-Q. Yang, *ACS Appl. Mater. Interfaces* **2013**, *6*, 1219.

[49] L. Wang, T. Maxisch, G. Ceder, *Phys. Rev. B* **2006**, *73*, 195107.

[50] D. Qian, B. Xu, M. Chi, Y. S. Meng, *Phys. Chem. Chem. Phys.* DOI:10.1039/C4CP01799D.

[51] Y. Dai, S. Ni, Z. Li, J. Yang, *J. Phys. Condens. Condensed Matter* **2013**, *25*, 405301.

[52] D. Young, *Computational chemistry: a practical guide for applying techniques to real world problems*, Wiley, New York **2001**.

[53] J. Maier, *Nat. Mater.* **2005**, *4*, 805.

[54] J. Reed, G. Ceder, *Chem. Rev.* **2004**, *104*, 4513.

[55] S. Kim, X. Ma, S. P. Ong, G. Ceder, *Phys. Chem. Chem. Phys.* **2012**, *14*, 15571.

[56] J. Bréger, Y. S. Meng, Y. Hinuma, S. Kumar, K. Kang, Y. Shao-Horn, G. Ceder, C. P. Grey, *Chem. Mater.* **2006**, *18*, 4768.

[57] D. Y. Yu, K. Yanagida, Y. Kato, H. Nakamura, *J. Electrochem. Soc.* **2009**, *156*, A417.

[58] M. Gu, I. Belharouak, J. Zheng, H. Wu, J. Xiao, A. Genc, K. Amine, S. Thevuthasan, D. R. Baer, J.-G. Zhang, N. D. Browning, J. Liu, C. Wang, *ACS Nano* **2013**, *7*, 760.

[59] Y. Okamoto, *J. Electrochem. Soc.* **2011**, *159*, A152.